Chalcogenide Letters Vol. 21, No. 3, March 2024, p. 229 - 241

Numerical simulation of Sb_2Se_3-based solar cells

S. H. Liu[a], J. R. Yuan[a,*], Y. Wu[a], X. H. Deng[a], Q. M. Yu[b]
[a]*School of Physics and Materials Science, Nanchang University, Nanchang 330031, China*
[b]*School of Chemistry and Chemical Engineering, Nanchang University, Nanchang 330031, China*

Antimony selenide (Sb_2Se_3) has remarkable optoelectronic capabilities that make it a promising option for the next generation solar cells. In this work, a solar cell with the structure Al/FTO/CdS/Sb_2Se_3/Mo is modeled and numerically analyzed using SCAPS-1D program. Furthermore, a Al/FTO/CdS/Sb_2Se_3/Sb_2S_3/Mo solar cell structure that uses Sb_2S_3 as the back surface field (BSF) layer is proposed. A comprehensive examination of photovoltaic characteristics for the solar cells was carried out. The optimization process involved adjusting the operating temperature, series and shunt resistance, doping concentration, bulk defect density, back contact metal work function, and thickness of the absorber layer. The optimized Sb_2Se_3-based solar cell with Sb_2S_3 material showed a conversion efficiency of 28.91%, suggesting that Sb_2Se_3-based solar cells have a great deal of potential for further development.

(Received December 16, 2023; Accepted March 4, 2024)

Keywords: Antimony selenide, Solar cells, SCAPS-1D, Conversion efficiency

1. Introduction

As fossil energy resources continue to deplete and environmental pollution intensifies, there is an urgent quest for clean and renewable energy sources. Thin-film solar cells, owing to their advantages such as minimal raw material consumption, simple preparation processes, and the material exhibits flexibility, have garnered increasing attention in recent years [1]. Notably, CIGS and CdTe photovoltaic cells have achieved industrial-scale production, while the laboratory efficiency of perovskite thin-film solar cells is comparable to that of crystalline silicon solar cells. However, the presence of rare elements such as indium and gallium in CIGS, the toxicity associated with cadmium in cadmium telluride, and the imperative need to enhance the stability of perovskite thin-film solar cells pose constraints on the further development of thin-film solar cell technologies [2-6]. In recent years, the p-type semiconductor Sb_2Se_3 has become the focus of widespread attention in the scientific community. This material boasts numerous advantages, including an appropriate bandgap, rational charge carrier mobility, high absorption coefficients, [1]abundant elements in the earth's crust, and non-toxicity [7-10]. Consequently, it holds the potential to serve as an absorber layer material for solar cells. Through the Shockley-Queisser limit theory, we can calculate that the photovoltaic conversion efficiency of Sb_2Se_3-based solar cells could theoretically reach a maximum of approximately 32% [11]. In previous endeavors to enhance the performance of Sb_2Se_3-based solar cells, researchers have devised and refined numerous device structures. The efficiency of cells employing a CdS/Sb_2Se_3 configuration reached 7.6% [12]. Experimental conversion efficiency for cells adopting the structure ZnO:Al/ZnO/CdS/TiO_2/Sb_2Se_3 nanorod arrays/$MoSe_2$/Mo amounted to 9.2% [13]. Theoretical conversion efficiency for solar cells with the FTO/CdS/Sb_2Se_3/Au configuration reached 16.5% [14]. Within the structure of Sb_2Se_3-based thin-film solar cells ITO/ZnO/CdS/Sb_2Se_3/CNT, with carbon nanotubes (CNT) serving as the back contact, a theoretical optimum efficiency of 21.67% was achieved [15]. In the configuration of FTO/CdS/Sb_2Se_3/HTL/Au solar cells, utilizing CuO as the hole transport layer (HTL), the theoretical efficiency reached 23.18% [16]. However, when compared to some other thin-film solar cells, Sb_2Se_3-based thin-film solar cells lack sufficient competitive advantages in terms of conversion efficiency and other performance metrics. Hence, there remains a need to design high-efficiency, low-cost Sb_2Se_3-based thin-film solar cells.

* Corresponding author: yuanjiren@ncu.edu.cn
https://doi.org/10.15251/CL.2024.213.229

Numerous factors impact the performance of solar cells, including doping concentration, absorber layer thickness, work function of the back contact electrode, operating temperature, and carrier recombination loss. Prior studies have demonstrated that the application of a BSF layer to the back of the absorber layer can substantially minimize the back surface recombination loss, consequently improving overall cell performance and conversion efficiency [17-18]. Because of its high absorption coefficient (>5×10^4 cm^{-1}) and suitable bandgap (~1.6 eV), Sb_2S_3 is the ideal material for the BSF layer in Sb_2Se_3-based thin-film solar cells. To optimize Sb_2Se_3-based solar cells, this study proposes a structure incorporating Sb_2S_3 as the BSF layer. The SCAPS-1D software is employed in this work to compare the performance of Sb_2Se_3-based solar cells with and without the inclusion of a BSF layer.

2. Device structure and simulation methodology

2.1. Device structure

The device structure employed in this simulation comprises Al/FTO/CdS/Sb_2Se_3/Mo, as illustrated in Fig. 1(a). Herein, the p-type semiconductor Sb_2Se_3 is used as the absorber layer, the n-type semiconductor CdS is served as the buffer layer, SnO_2:F (FTO) is acted as the window layer, and molybdenum (Mo) and aluminum (Al) are served as the back contact and front contact, respectively. Al has a metal work function of 4.08 eV [19], while Mo has a metal work function of 4.95 eV[20]. In the aforementioned configuration, we have introduced Sb_2S_3 as the BSF layer as depicted in Figure 1(b). This addition aims to mitigate carrier recombination loss in the solar cell while enhancing the collection of photogenerated carriers.

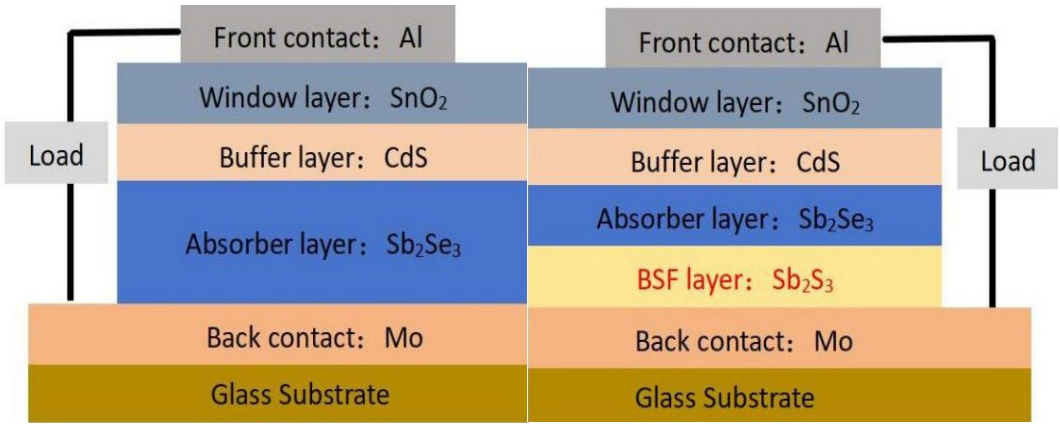

(a) *(b)*

Fig. 1. Schematic structure of the studied Sb_2Se_3 solar cells: (a) basic Al/FTO/CdS/Sb_2Se_3/Mo (without BSF layer) cell and (b) proposed cell Al/FTO/CdS/Sb_2Se_3/Sb_2S_3/Mo (with BSF layer).

2.2. Simulation methodology

In the exploration of thin-film solar cell performance, researchers widely employ various software tools, such as AMPS, COMSOL, wxAMPS and SCAPS-1D. For this study, we have opted for SCAPS-1D. This software serves as a one-dimensional solar cell simulator, utilized for modeling the performance and various crucial parameters of solar cells[21]. The program is based on numerical solutions for the fundamental semiconductor equations, Poisson equation, and continuity equation (Equations (1)-(3))[22], utilized for the computation of performance parameters in Sb_2Se_3-based solar cells.

$$\frac{\partial^2\Psi}{\partial x^2} + \frac{q}{\varepsilon}[p(x) - n(x) + N_D - N_A + \rho_p - \rho_n] = 0 \quad (1)$$

$$\frac{1}{q}\frac{dJ_p}{dx} = G_{op}(x) - R(x) \quad (2)$$

$$\frac{1}{q}\frac{dJ_n}{dx} = -G_{op}(x) + R(x) \quad (3)$$

In the equations presented, ε is dielectric constant, q represents the charge of an electron, N_A and N_D denote the acceptor and donor densities, Ψ signifies the electrostatic potential, p and n stand for hole and electron concentrations, ρ_p and ρ_n represent hole and electron distribution, and Jp and Jn denote hole current density and electron current density, respectively. $G_{op}(x)$ is the optical generation rate, and R(x) net combination rate. All these parameters are functions of the spatial coordinate x. SCAPS partitions a solar cell structure into slab and main grid points, discretizing the aforementioned differential equations into sets of algebraic equations [21-22]. The open-circuit voltage (V_{oc}), short-circuit current (J_{sc}), fill factor (FF), conversion efficiency (η), band diagram, I-V characteristics, and other solar cell parameters can all be computed using the solutions to these equations.

2.3. Simulation parameters

A comprehensive summary of key parameters is provided in Tables 1 and 2, collating data from literature and experimental results [19-22]. Throughout all simulations, we utilized illumination with a front light intensity of 1000 W/m^2 and AM1.5G spectrum, maintaining a temperature of 300 K. The absorption coefficient of Sb_2Se_3 is set to 10^5 cm^{-1} [22], In each layer of materials, the approximate thermal velocities of the holes and electrons are 10^7 cm/s at room temperature [19]. The surface recombination velocities of electrons and holes for Mo and Al are both 10^7 cm/s. The energy levels of defects are modeled as a neutral Gaussian distribution with a characteristic energy of 0.1 eV [22].

Table 1. Simulation parameters for the Sb_2Se_3-based solar cell.

Material Properties	SnO_2	CdS	Sb_2Se_3	Sb_2S_3
Thickness (μm)	0.05	0.05	1.0*	0.05
Band gap (eV)	3.6	2.4	1.09	1.62
Electron affinity (eV)	4	4.2	3.9	3.7
Dielectric permittivity	9	10	18	9.00
Conductor band effective density of states (cm^{-3})	2.2×10^{18}	2.2×10^{18}	2.2×10^{18}	2.2×10^{18}
Value band effective density of states (cm^{-3})	1.8×10^{19}	1.8×10^{19}	1.8×10^{19}	1.8×10^{19}
Electron thermal velocity (cm/s)	1×10^7	1×10^7	1×10^7	1×10^7
Hole thermal velocity (cm/s)	1×10^7	1×10^7	1×10^7	1×10^7
Electron mobility (cm^2 /Vs)	100	100	15	9.8
Hole mobility (cm^2 /Vs)	25	25	5.1	10
Shallow uniform donor density N_D (cm^{-3})	1×10^{18}	1×10^{17}	0	0
Shallow uniform acceptor density N_A (cm^{-3})	0	0	1×10^{17}*	1×10^{18}
Defect type	Single Acceptor	Single Acceptor	Single Donor	Single Donor
Energetic distribution	Gaussian	Gaussian	Gaussian	Gaussian
Defect density (cm^{-3})	1×10^{15}	1×10^{15}	1×10^{14}	1×10^{15}

Note: * is a variable field.

Table 2. Interface parameters used in the FTO/CdS/Sb_2Se_3/Sb_2S_3 heterojunction device Simulation.

Parameters	CdS/Sb_2Se_3 interface	Sb_2Se_3/Sb_2S_3 interface
Defect type	Neutral	Neutral
Capture cross-section of electrons (cm^2)	1×10^{-19}	1×10^{-19}
Capture cross-section of holes (cm^2)	1×10^{-19}	1×10^{-19}
Reference for defect energy level Et	above the highest Ev	above the highest Ev
Energy with respect to Reference (eV)	0.01	0.01
Total density (cm^{-2})	1×10^{10}	1×10^{10}

3. Results and discussion

In this study, our focal point lies in investigating the impact of various parameters of the absorber layer on the performance of Sb_2Se_3-based TFSCs. We employ SCAPS-1D software for simulation, exploring the effects of Sb_2Se_3 absorber layer thickness, doping concentration, bulk defect density, as well as the back contact metal work function, operating temperature, and series and parallel resistances of the solar cell on the performance of Sb_2Se_3-based solar cells. Simultaneously, we conduct a comparative analysis, examining parameters such as V_{oc}, J_{sc}, FF, and η for Sb_2Se_3-based solar cells with and without an Sb_2S_3 BSF layer under identical conditions. Furthermore, we optimize various parameters of the solar cell based on this comparison. Utilizing the optimized data, we delve into the J-V characteristics, band diagrams, built-in electric fields, and other aspects of the cell, This facilitates the creation of solar cell structures with higher efficiency.

3.1. Energy band diagram

Fig. 2 illustrates the band structure of Sb_2Se_3-based solar cells with Sb_2S_3 as the BSF layer. At the interface of Sb_2Se_3/CdS, photo-generated charge carriers are effectively separated and rapidly accelerated away from the interface of Sb_2Se_3/CdS under the influence of the electric field. Holes traverse the Sb_2Se_3 absorber layer, being collected by the metallic Mo, while electrons flow into the CdS buffer layer. From the diagram, it is evident that in this simulated study, each layer's thickness and bandgap are discernible. We observe the formation of a p^+-Sb_2S_3/p-Sb_2Se_3 heterojunction between the Sb_2S_3 BSF layer and the Sb_2Se_3 absorber layer. Consequently, a potential barrier is established at the interface of the Sb_2S_3 BSF layer and the Sb_2Se_3 absorber layer, aiding in impeding the flow of electrons to the back surface of the solar cell. This potential barrier formation contributes to mitigating carrier recombination loss in the solar cell[19].

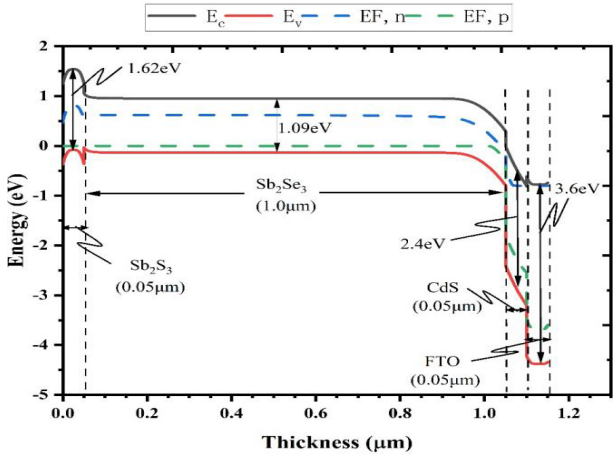

Fig. 2. Band diagram of Sb_2Se_3-based solar cell with BSF layer.

3.2. Effect of absorber layer thickness on the device

The performance of the solar cells is influenced by the thickness of the absorption layer, encompassing the fill factor and conversion efficiency. When the absorption layer is excessively thin, the solar cell fails to fully capture all incident light, resulting in a decline in cell efficiency, as explicitly depicted in Formula (4):

$$a(\lambda, W) = 1 - e^{(-2a(\lambda)W)} \tag{4}$$

Here, W represents the thickness of the solar cell, λ is the wavelength of absorbed light, and $a(\lambda)$ denotes the absorption of light with wavelength λ [22]. Insufficient thickness of the absorption layer results in an inability to capture all incident light, consequently leading to a decrease in efficiency [23]. Fig. 3 illustrates the impact of varying the thickness of the Sb_2Se_3 absorber layer, ranging from 0.1 μm to 2 μm, on the performance parameters of Sb_2Se_3-based TFSCs. Additionally, we conducted a comparative analysis between solar cells with and without a Sb_2S_3 BSF layer to examine its influence.

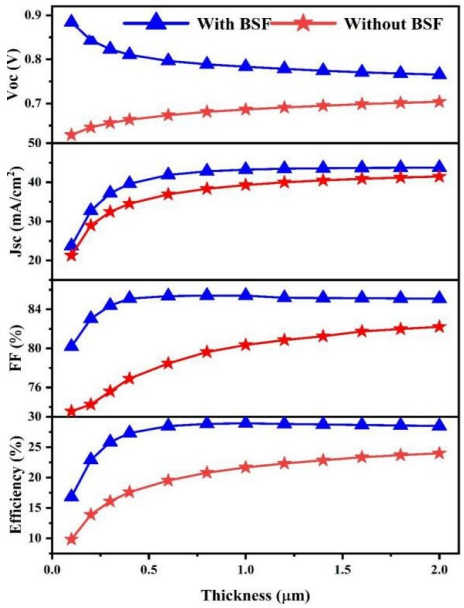

Fig. 3. Effect of the absorber layer thickness on the parameters of the solar cell (V_{oc}, J_{sc}, η, FF).

Throughout this process, we maintained constant values for other parameters. Through simulation, we derived the solar cell's V_{oc}, J_{sc}, FF, and η to explore the effects of absorber layer thickness on solar cell performance.

In thin-film solar cells (TFSCs) without the Sb_2S_3 BSF layer, we observe an ascending trend in the V_{oc}, J_{sc}, FF, and η as the absorber layer thickness increases. However, beyond a thickness of 1 μm, the upward trajectory of these parameters begins to plateau. At an absorber layer thickness of 0.1 μm, V_{oc} is 0.63V, J_{sc} is 21.25 mA/cm², FF is 73.56%, and η is 9.83%. As the thickness increases to 2 μm, V_{oc} becomes 0.7V, J_{sc} reaches 41.46 mA/cm², and FF and η attain values of 82.21% and 23.99%, respectively. In Sb_2Se_3-based solar cells with the inclusion of the Sb_2S_3 BSF layer, at an absorber layer thickness of 0.1 μm, the FF is 80.18%, and η is 16.8%. With increasing thickness, FF and η continue to rise. After reaching a thickness of 0.5 μm, the upward trend in FF and η begins to decelerate. At an absorber layer thickness of 1 μm, the solar cell achieves maximum FF and η values, reaching 85.4% and 28.91%, respectively. The impact of absorber layer thickness on solar cell performance primarily manifests in two aspects: the collection of photons and the efficiency of charge carrier transmission. With a thinner absorber layer, the impediment to charge carrier transmission within the cell is minimal, and photon absorption plays a dominant role in solar cell performance. As the absorber layer thickness increases, the number of absorbed photons also increases, thereby enhancing the solar cell's performance. However, as the absorber layer thickness continues to rise, the efficiency of charge carrier transmission becomes pivotal in determining the FF and conversion efficiency of the solar cell. The increase in absorber layer thickness results in a longer path for charge carrier transmission, leading to partial recombination losses during the transmission process, thereby affecting solar cell performance. Under the combined influence of these factors, selecting an appropriate absorber layer thickness becomes crucial for optimizing solar cell performance. As the absorber layer thickness increases, the recombination rate of charge carriers exceeds the generation rate, causing J_{sc} to approach saturation.

Through comparative analysis, we discern that, during the transition from an absorber layer thickness of 0.1 μm to 2.0 μm, the performance of Sb_2Se_3-based solar cells with the inclusion of the Sb_2S_3 BSF layer consistently surpasses that of solar cells lacking the Sb_2S_3 buffer layer. At a thickness of 1.0 μm, the solar cell with the BSF layer exhibits a V_{oc} of 0.78V, J_{sc} of 43.22 mA/cm², FF of 85.4%, and an efficiency of 28.91%. In contrast, the Sb_2Se_3-based TFSCs without the BSF layer displays a Voc of 0.68V, Jsc of 39.28 mA/cm², FF of 80.34%, and an efficiency of 21.66%. The introduction of the Sb_2S_3 BSF layer results in the formation of a p^+-Sb_2S_3/p-Sb_2Se_3 heterojunction, creating a distinctive electric field at the interface between the absorber layer and the BSF layer, as depicted in Fig. 4.This electric field hinders the passage of minority carriers from the backside of the solar cell, effectively reducing recombination losses and diminishing dark current within the cell. Additionally, the reduction in dark current within the cell contributes to the elevation of J_{sc}, thereby enhancing the performance of the Sb_2Se_3-based thin-film solar cells [19,25]. Comparative studies reveal that the incorporation of the Sb_2S_3 BSF layer not only significantly improves the overall efficiency of the cell but also enables the attainment of higher V_{oc}, J_{sc}, FF, and η, even as the thickness of the absorber layer is minimized.

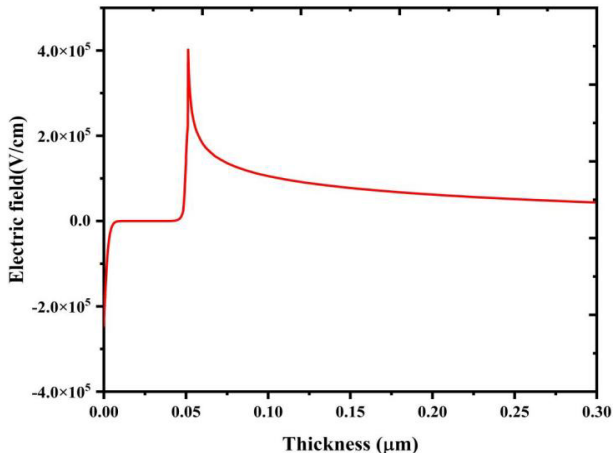

Fig. 4. The built-in electric field at the p^+-Sb_2S_3 / p-Sb_2Se_3 heterojunction

The reduction in absorber layer thickness not only enhances performance but also proves instrumental in diminishing material costs required for production. Consequently, the inclusion of the Sb_2S_3 BSF layer plays a pivotal role in achieving a thinner, more efficient Sb_2Se_3-based thin-film solar cells.

3.3. The impact of series resistance and parallel resistance on solar cell performance.

The complexity of series resistance, which is made up of several resistances, must be taken into account in order to fully comprehend the effects of shunt resistance (R_{sh}) and series resistance (R_s).For example, each layer of material within the cell contributes to resistance, there is resistance between semiconductor materials and the contact points with front and rear metals, and the metal electrode itself possesses resistance. These resistances collectively form the series resistance Rs. Simultaneously, the occurrence of shunt resistance is associated with reverse saturation current [26].To investigate the effects of R_s and R_{sh}, while keeping other parameters at their optimized values, we varied R_s and R_{sh} in the ranges of 0 to 21Ω-cm^2 and 10 to 300Ω-cm^2, respectively.

The effect of R_s and R_{sh} on the solar cell's performance is shown in Fig. 5. From Fig. 5, it can be observed that as R_s increases and R_{sh} decreases, the cell efficiency decreases from 27.31% to 1.51%. J_{sc} and FF gradually decrease, while the variation in V_{oc} is significantly influenced by R_{sh}, increasing from 0.43V to 0.78V. These observations indicate that high series resistance and low shunt resistance can significantly degrade the solar cell performance. Therefore, achieving low series resistance and high shunt resistance is imperative for realizing high efficiency and outstanding performance in solar cells.

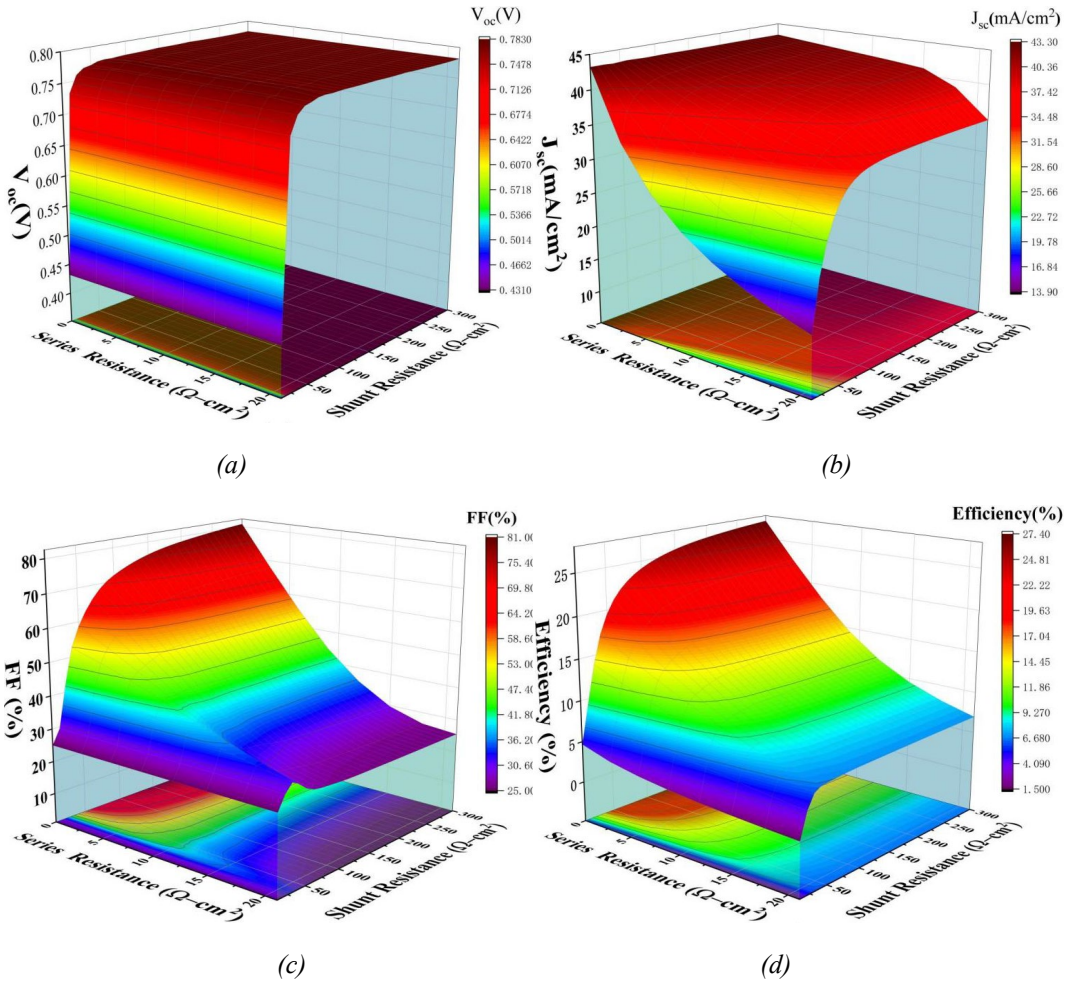

Fig. 5. The influence of series resistance and parallel resistance on the parameters of the solar cell (V_{oc}, J_{sc}, FF, η).

Furthermore, this study reveals that lower R_{sh} results in a reduction in V_{oc} and J_{sc}, consequently lowering the maximum power of the cell and ultimately affecting efficiency and fill factor. Thus, this research underscores the crucial impact of series resistance and shunt resistance on the cell performance.

3.4. Current density-voltage characteristics

Fig. 6(a) illustrates the I-V characteristics of two solar cell structures. In the absence of illumination, the energy supply to the cell emanates from the externally applied voltage. The diffusion current generated by the majority charge carriers exhibits exponential growth under the influence of external voltage, displaying characteristics akin to a diode. Under illuminated conditions, the energy supply of the cell originates from internally generated photo-generated carriers. The increased abundance of minority charge carriers, facilitated by their drift, results in a substantial current density. Hence, we consider that the fundamental mechanisms governing current transmission in solar cells involve the diffusion and drift of carriers [19,27].

Fig. 6(b) depicts the C-V characteristics of the two solar cell structures. Beyond a voltage threshold of 0.5V, the capacitance experiences rapid ascent. Notably, solar cells incorporating an Sb_2S_3 BSF layer exhibit a swifter rise in capacitance. A greater rate of change in capacitance with voltage amplifies the differential capacitance, promoting faster drift and response of photogenerated carriers, thereby contributing to the enhancement of solar cell performance.

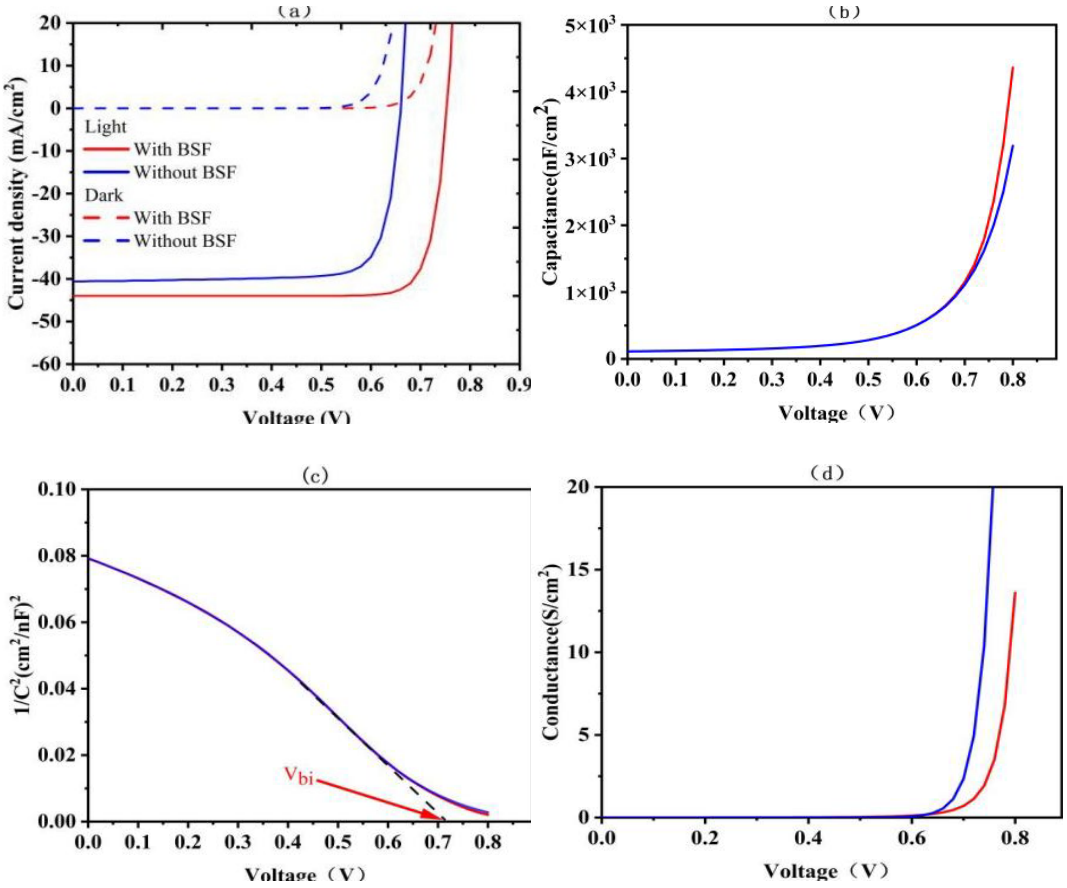

Fig. 6. (a)J-V characteristic, (b)C-V characteristic, (c) Mott - Schottky plot, (d) Conductance-Voltage characteristic.

Figure 6(c) depicts the Mott-Schottky curves of the solar cells, from which we can deduce that the built-in potential (V_{bi}) for both types of cells is 0.72V.A higher V_{bi} accentuates the depletion layer in the cell, facilitating the absorption of photons and the generation of electron-hole pairs[28-29]. Moreover, V_{bi} directly impacts the V_{oc}, J_{sc}, FF, thereby exerting a significant

influence on the conversion efficiency of solar cells. Fig. 6(d) illustrates the variation of conductance with voltage. Post 0.6V, conductance undergoes rapid augmentation. Comparative analysis indicates that the introduction of an Sb_2S_3 BSF layer results in a notable enhancement in both the I-V and C-V characteristics of solar cells, significantly contributing to improvements in V_{oc}, J_{sc}, FF, and η.

3.5. Effect of the variation in the concentration of shallow acceptor density

Fig. 7 illustrates the impact of the carrier concentration in the absorber layer, ranging from 1×10^{12} to 1×10^{17} cm^{-3}, on the V_{oc}, J_{sc}, FF, and η of Sb_2Se_3-based TFSCs with an Sb_2S_3 BSF layer. It is observed that Jsc remains nearly constant throughout this process. However, as the carrier concentration increases, the TSA conversion process in the BSF layer is affected, leading to a slight decrease in J_{sc} [30-31]. With the rise in carrier concentration, V_{bi} also increases, resulting in a reduction in the internal recombination current within the cell [32]. Consequently, the V_{oc}, FF, and η of the solar cell are influenced. As the carrier concentration in the absorber layer increases from 1×10^{12} to 1×10^{17} cm^{-3}, V_{oc} rises from 0.72 to 0.78V. The fill factor and conversion efficiency also increase from 76.3% and 24.08% to 85.4% and 28.91%, respectively.

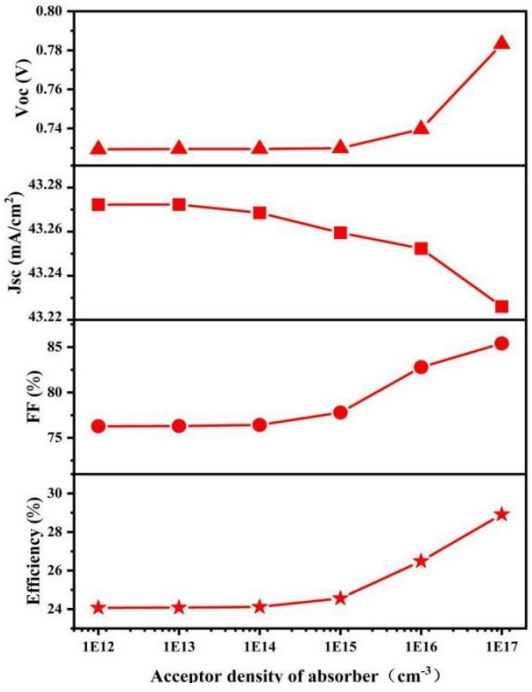

Fig. 7. The influence of carrier concentration in Sb_2Se_3 absorber layer on various parameters of solar cell (V_{oc}, J_{sc}, FF, η).

3.6. Effect of variation in back contact work function

The back contact work function has a significantly impact on solar cells' efficiency. In order to avoid the formation of a Schottky junction at the interface, the back contact metals for Sb_2Se_3-based solar devices, such as Au, Ag, Mo, and Pt, among others, are expected to have work functions greater than 4.8 eV [33].Fig. 8. depicts the influence of the back contact work function on the conversion efficiency of solar cells. In our experiments, we adjusted the back contact work function between 4.7 and 5.1 eV in order to evaluate the performance of the solar cell. However, the efficiency of the cell stopped showing appreciable growth once the work function reached 4.95 eV. We chose Mo, whose work function is 4.95 eV, as the back contact in order to optimize the solar cell's structure and performance. This decision enhances the performance of the cell.

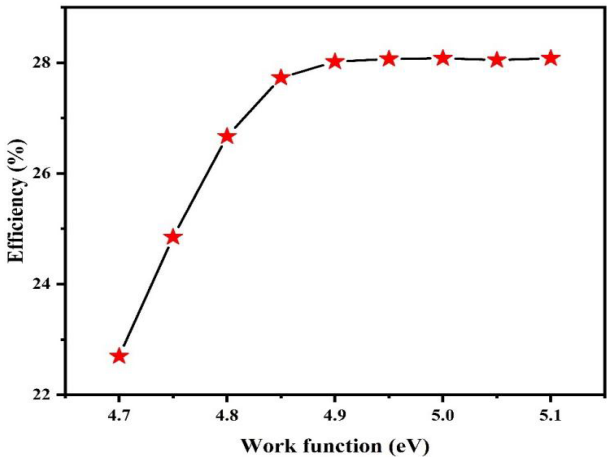

Fig. 8. Effect of back contact work function on the conversion efficiency of Sb_2Se_3-based solar cells containing a BSF layer.

3.7 Effect of variation in the concentration of defect density

Fig. 9 demonstrates the impact of the defect density in the absorber layer on the output parameters of Sb_2Se_3-based solar cells with a BSF layer. Throughout the simulation process, other parameters were maintained at their optimized values, while the defect density varied from 1×10^{13} to 1×10^{17} cm^{-3}. It is observed that with the increase in defect density, both V_{oc} and J_{sc} gradually decrease. Conversely, FF initially increases, reaching a maximum of 85.19% at a defect density of 1×10^{14} cm^{-3}, and then steadily decreases. At defect densities of 1×10^{14} cm^{-3} and 1×10^{17} cm^{-3}, the efficiency of the solar cell is 28.91% and 10.69%, respectively. As the photo-generated current is primarily produced by the Sb_2Se_3 absorber layer, an increase in defect density leads to a reduction in carrier lifetime and diffusion length, resulting in carrier recombination losses and a substantial decrease in solar cell efficiency [34]. Through our investigation, we ascertain that a high defect density in the absorber layer significantly diminishes the output parameters of the solar cell. To optimize the Sb_2Se_3-based solar cell, we choose a defect density of 1×10^{14} cm^{-3}, at which point the cell achieves a conversion efficiency of 28.91%.

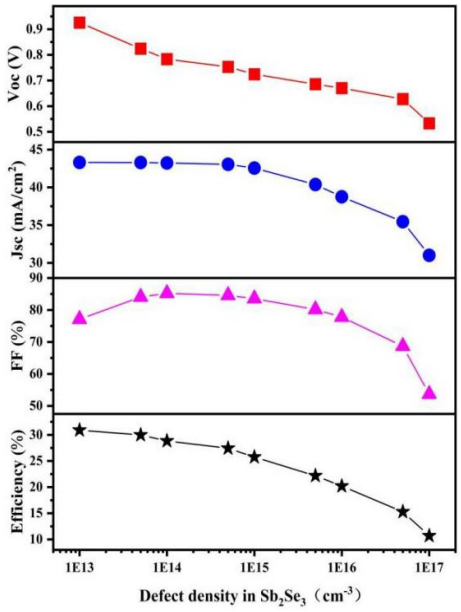

Fig. 9. Effect of defect density of absorber layer on various parameters of solar cell (Voc, Js c, FF, η).

3.8. Effect of absorber layer temperature on the device

To validate the stability of the proposed Sb_2Se_3-based solar cell, we conducted a detailed analysis of the influence of operating temperature in the range of 250 to 450 K on the cell performance. In this numerical study, all other parameters remained constant, as specified in Table 1. Figure 10 illustrates the performance parameters of Sb_2Se_3-based solar cells, both without a BSF and with an Sb_2S_3 BSF layer, at different operating temperatures, including V_{oc}, J_{sc}, FF, and efficiency.

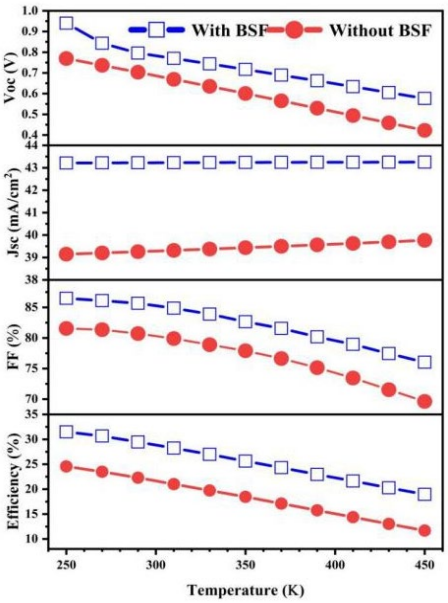

Fig. 10. The effect of temperature on the parameters of the solar cell (V_{oc}, J_{sc}, FF, η).

It is observed from Fig. 10 that the V_{oc}, J_{sc}, FF, and efficiency exhibit a decreasing trend , as the temperature increases. The results indicate that, compared to solar cells without a BSF layer, those with an Sb_2S_3 BSF layer demonstrate superior performance. The V_{oc} of the cell gradually decreases with rising temperature. It is attributed to enhance reverse saturation current caused by temperature elevation. Alongside an increase in series resistance and a reduction in carrier diffusion length, the cell generates more interface defects. With an increase in temperature, the material bandgap decreases, resulting in a minor upward trend in Jsc for the cell [27].At 250 K, the conversion efficiency of the solar cell with a BSF layer is 31.48%; at 450 K, the efficiency decreases to 18.96%. This decrease is attributed to the impact of elevated temperature on the mobility of holes and electrons, as well as the concentration of carriers, resulting in a overall decrease in the solar cell efficiency [26].

4. Conclusion

In this study, we utilized the SCAPS-1D software to investigate the performance of Sb_2Se_3-based thin-film solar cells. We proposed the Sb_2S_3 as a back surface field (BSF) layer for traditional Sb_2Se_3-based solar cells. We conducted a comparative analysis, studying the impact of absorber layer thickness, bulk defect density in the absorber layer, doping concentration, environmental temperature, back contact work function, and series-parallel resistance on the performance of Sb_2Se_3-based TFSCs with and without the Sb_2S_3 BSF layer. The results indicate that incorporating the Sb_2S_3 BSF layer in traditional Sb_2Se_3-based solar cells effectively reduces internal carrier recombination losses, thereby enhancing open-circuit voltage, current density, fill factor, and conversion efficiency. Maintaining other parameters constant, the addition of an Sb_2S_3 BSF layer to traditional Sb_2Se_3-based solar cells increases the conversion efficiency from 21.66%

to 28.91%. In addition, the addition of Sb_2S_3 can improve the solar cell performance in a number of ways while reducing the thickness of the absorber layer and optimizing the cell structure. The optimized solar cell parameters include a 1.0 μm thick Sb_2Se_3 absorber layer, a 0.05μm thick Sb_2S_3 BSF layer, and a carrier concentration of 1×10^{17} cm^{-3} in the Sb_2Se_3 absorber layer. When the bulk defect density in the absorber layer decreases to 1×10^{14} cm^{-3}, the Sb_2Se_3-based solar cell achieves an optimal conversion efficiency of 28.91%, with V_{oc} of 0.78 V, J_{sc} of 43.22 mA/cm^2, and FF of 85.4%. The introduction of the Sb_2S_3 BSF layer also improves the cell performance and stability of Sb_2Se_3-based thin-film solar cells. These results suggest significant potential for the development of Sb_2Se_3-based solar cells, and numerical simulations can contribute to the creation of low-cost, high-efficiency thin-film solar cells based on Sb_2Se_3.

Acknowledgements

This work was supported by the National Natural Science Foundation of China (No. 11964018) and the Natural Science Foundation of Jiangxi Province of China (Grant No. 20224BAB202032). The authors acknowledge the use of the SCAPS-1D program developed by Prof. Burgelman's group of the University of Gent, Belgium.

References

[1] H. Jalali, A. A. Orouji, I. Gharibshahian, Solar Energy Materials and Solar Cells **260**, 112492 (2023); https://doi.org/10.1016/j.solmat.2023.112492
[2] S. Abbas, S. Bajgai, S. Chowdhury, A. S. Najm, M. S. Jamal, K. Techato, S. Channumsin, S. Sreesawet, M. Channumsin, A. Laref, Materials **15**(18), 6272 (2022); https://doi.org/10.3390/ma15186272
[3] K. K. Maurya, V. N. Singh, Heliyon **8**(10), e10925 (2022); https://doi.org/10.1016/j.heliyon.2022.e10925
[4] Y. Singh, K. K. Maurya, V. N. Singh, Mater. Today Sustainability **18**, 100148 (2022); https://doi.org/10.1016/j.mtsust.2022.100148
[5] M. D. Chatzisideris, N. Espinosa, A. Laurent, F. C. Krebs, Solar Energy Materials and Solar Cells **156**, 2 (2016); https://doi.org/10.1016/j.solmat.2016.05.048
[6] K. K. Maurya, V. N. Singh, J. Sci.:-Adv. Mater. Device. **7**(2), 100445 (2022); https://doi.org/10.1016/j.jsamd.2022.100445
[7] S. Chowdhury, A. S. Najm, M. Luengchavanon, A. M. Holi, C. H. Chia, K. Techato, S. Channumsin, I. K. Salih, Energ Fuel **37**(9), 6722 (2023); https://doi.org/10.1021/acs.energyfuels.2c03593
[8] Y. Zhou, L. Wang, S. Chen, S. Qin, X. Liu, J. Chen, D.-J. Xue, M. Luo, Y. Cao, Y. Cheng, E. H. Sargent, J. Tang, Nat. Photonics **9**(6), 409 (2015); https://doi.org/10.1038/nphoton.2015.78
[9] C. Chen, W. Li, Y. Zhou, C. Chen, M. Luo, X. Liu, K. Zeng, B. Yang, C. Zhang, J. Han, Appl. Phys. Lett. **107**(4), 043905 (2015); https://doi.org/10.1063/1.4927741
[10] A. Ait Abdelkadir, M. Sahal, E. Oublal, N. Kumar, A. Benami, Opt. Quantum Electron. **55**(6), 514 (2023); https://doi.org/10.1007/s11082-023-04797-7
[11] S. Rühle, Sol. Energy **130**, 139 (2016); https://doi.org/10.1016/j.solener.2016.02.015
[12] X. Wen, C. Chen, S. Lu, K. Li, R. Kondrotas, Y. Zhao, W. Chen, L. Gao, C. Wang, J. Zhang, G. Niu, J. Tang, Nat. Commun. **9**(1), 2179 (2018); https://doi.org/10.1038/s41467-018-04634-6
[13] Z. Li, X. Liang, G. Li, H. Liu, H. Zhang, J. Guo, J. Chen, K. Shen, X. San, W. Yu, R. E. I. Schropp, Y. Mai, Nat. Commun. **10**(1), 125 (2019); https://doi.org/10.1038/s41467-018-07903-6
[14] L.-y. Lin, L.-q. Jiang, Y. Qiu, B.-d. Fan, J. Phys. Chem. Solids **122**, 19 (2018); https://doi.org/10.1016/j.jpcs.2018.05.045
[15] F. Baig, Y. H. Khattak, B. M. Soucase, S. Beg, S. R. Gillani, S. Ahmed, J. Nanoelectron. Optoelectron. **14**(1), 72 (2019); https://doi.org/10.1166/jno.2019.2451
[16] Z.-Q. Li, M. Ni, X.-D. Feng, Mater. Res. Express **7**(1), 016416 (2020); https://doi.org/10.1088/2053-1591/ab5fa7
[17] M. S. Rana, M. M. Islam, M. Julkarnain, Sol. Energy **226**, 272 (2021); https://doi.org/10.1016/j.solener.2021.08.035

[18] S. Souri, M. Marandi, Opt. Quantum Electron. **55**(5), 397 (2023); https://doi.org/10.1007/s11082-023-04563-9
[19] S. R. Al Ahmed, A. Sunny, S. Rahman, Solar Energy Materials and Solar Cells **221**, 110919 (2021); https://doi.org/10.1016/j.solmat.2020.110919
[20] K. K. Maurya, V. N. Singh, Sol. Energy **228**, 540 (2021); https://doi.org/10.1016/j.solener.2021.09.080
[21] A. Basak, U. P. Singh, Solar Energy Materials and Solar Cells **230**, 111184 (2021); https://doi.org/10.1016/j.solmat.2021.111184
[22] K. K. Maurya, V. N. Singh, Sol. Energy **230**, 803 (2021); https://doi.org/10.1016/j.solener.2021.11.002
[23] R. T. Mouchou, T. C. Jen, O. T. Laseinde, K. O. Ukoba, Mater. Today-Proc. **38**, 835 (2021); https://doi.org/10.1016/j.matpr.2020.04.880
[24] R. Kumari, Mamta, A. K. Chaudhary, V. N. Singh, Adv. Theor. Simul., 2300322 (2023); https://doi.org/10.1002/adts.202300322
[25] I. Gharibshahian, A. A. Orouji, S. Sharbati, Solar Energy Materials and Solar Cells **212**, 110581 (2020); https://doi.org/10.1016/j.solmat.2020.110581
[26] H. Heriche, Z. Rouabah, N. Bouarissa, Int. J. Hydrogen Energy **42**(15), 9524 (2017); https://doi.org/10.1016/j.ijhydene.2017.02.099
[27] A. Laidouci, A. Aissat, J. P. Vilcot, Sol. Energy **211**, 237 (2020); https://doi.org/10.1016/j.solener.2020.09.025
[28] B. K. Mondal, S. K. Mostaque, M. A. Rashid, A. Kuddus, H. Shirai, J. Hossain, Superlattices Microstruct. **152**, 106853 (2021); https://doi.org/10.1016/j.spmi.2021.106853
[29] P. Kumari, U. Punia, D. Sharma, A. Srivastava, S. K. Srivastava, Silicon **15**(5), 2099 (2023); https://doi.org/10.1007/s12633-022-02163-y
[30] B. K. Mondal, S. K. Mostaque, J. Hossain, Heliyon **8**(3), e09120 (2022); https://doi.org/10.1016/j.heliyon.2022.e09120
[31] A. Kuddus, A. B. M. Ismail, J. Hossain, Sol. Energy **221**, 488 (2021); https://doi.org/ 10.1016/j.solener.2021.04.062
[32] J. Hossain, M. Rahman, M. M. A. Moon, B. K. Mondal, M. F. Rahman, M. H. K. Rubel, Eng. Res. Express **2**(4), 045019 (2020); https://doi.org/10.1088/2631-8695/abc56c
[33] Mamta, R. Kumari, R. Kumar, K. K. Maurya, V. N. Singh, Sustainability **15**(13), 10465 (2023); https://doi.org/10.3390/su151310465
[34] S. R. I. Biplab, M. H. Ali, M. M. A. Moon, M. F. Pervez, M. F. Rahman, J. Hossain, J. Comput. Electron. **19**(1), 342 (2020); https://doi.org/10.1007/s10825-019-01433-0